

Fully Textile X-Ray Detectors Based on Fabric-Embedded Perovskite Crystals

Luca Possanzini, Laura Basiricò,* Andrea Ciavatti, Marta Tassarolo, and Beatrice Fraboni

The interest and thrust for wearable ionizing radiation dosimeters are rapidly growing, stimulated by a large number of different applications impacting on humankind, spanning from medicine to civil security and space missions. Lead halide perovskites are considered one of the most promising classes of novel materials for X-ray detectors due to their superior electronic and detection performance coupled with compatibility with solution-based printing processes, allowing fabrication onto flexible substrates. It is reported on fully textile perovskite-based direct X-ray detectors, where the photoactive layer is constituted by a silk-satin fabric functionalized with methylammonium lead bromide perovskite crystals embedded in the textile. The reliability of the proposed fabrication process, based on simple and low-tech deposition techniques adaptable to industrial printing technologies for textiles, is assessed by realizing different detector's architectures that exhibit comparable detection performances. Sensitivity values up to $(12.2 \pm 0.6) \mu\text{C Gy}^{-1} \text{cm}^{-2}$ and a limit of detection down to $3 \mu\text{Gy s}^{-1}$ are achieved, and low bias operation (down to 1 V) is demonstrated, validating wearable applications. Further, fully textile pixelated matrix X-ray sensors are implemented and tested, providing the proof of principle for large-area scalability.

properties due to an external stimulus, designed to measure biopotential,^[6–8] temperature,^[9] movements as pressure,^[10] or strain,^[11] sweat content,^[12–14] or as energy harvesting (thermoelectrics,^[15,16] triboelectrics,^[17] and biofuel cells^[18]), and storage platforms.^[19,20] The flexible, comfortable, and breathable nature of fabrics makes these substrates ideal candidates for developing large-area wearable devices in direct contact with the human body. Despite the high number of different textile sensors realized so far, textile ionizing radiation detectors have not been proposed yet, mostly due to the incompatibility between conventional materials for radiation sensing and fabric substrates. The development of innovative functional materials and low-cost technologies for the detection of ionizing radiations has become an urgent need in the last years due to the relevant increase in the use of ionizing radiation in many aspects of modern society, from medical applications


1. Introduction

“Wearable electronics” identifies an emerging category of technological devices that allow a passive, unobtrusive, and continuous monitoring of physiological or biometric parameters. Such sensors are integrated into bracelets, watches, headbands, skin patches, earphones, or garments and are mostly implemented on conventional substrates. Considerable interest in the research community is focused on devices realized directly onto textile substrates,^[1–5] as witnessed by electronic textile devices that can change their electrical and/or mechanical

to civil security. In particular, flexible and wearable innovative dosimeters are highly requested in hazardous environments, e.g., for personnel and patients in medical therapy and for space missions' crew. Commercially available personal dosimeters and diagnostic detectors, based on inorganic materials (e.g., silicon-based solid-state devices for dosimeters, a-Si, a-Se, or poly-cadmium zinc telluride for large-area flat panels) are heavy, bulky, rigid, and uncomfortable to be worn. Furthermore, they are difficult to implement in large, pixelated matrices by means of low-cost and low-tech fabrication techniques. In the last years, a new generation of X-ray detectors has been explored, based on organic semiconductors^[21–23] and perovskites,^[24–26] two classes of materials that allow for liquid phase deposition methods, enabling an easy device scaling up to large areas and the implementation on unconventional flexible substrates, such as thin plastic foils^[27,28] and even fabrics.^[29–31] Lead halide perovskites are an emerging and promising class of materials for X-ray detection, thanks to their utmost electric transport properties, (i.e., high charge carrier mobilities and long carrier lifetime), excellent optical properties, together with high ionizing radiation stopping power due to the presence of heavy atoms (e.g., Br, Pb, or I) in their molecular structure. The combination of all these features has led to impressive performance of lead halide perovskite devices in the direct detection of X-rays and gamma rays, both in films^[31] and single crystal forms.^[32–34] However, despite their excellent performance, single crystals retain a mechanical stiffness preventing the implementation

L. Possanzini, L. Basiricò, A. Ciavatti, M. Tassarolo, B. Fraboni
Department of Physics and Astronomy
University of Bologna
Viale Berti-Pichat 6/2, Bologna 40127, Italy
E-mail: laura.basirico2@unibo.it

L. Basiricò, A. Ciavatti, B. Fraboni
National Institute for Nuclear Physics—INFN Section of Bologna
Viale C. Berti Pichat 6/2
Bologna 40127, Italy

 The ORCID identification number(s) for the author(s) of this article can be found under <https://doi.org/10.1002/admi.202101417>.

© 2022 The Authors. Advanced Materials Interfaces published by Wiley-VCH GmbH. This is an open access article under the terms of the Creative Commons Attribution License, which permits use, distribution and reproduction in any medium, provided the original work is properly cited.

DOI: 10.1002/admi.202101417

of bendable devices. On the other hand, the growth of thick-film-based perovskite detectors requires high-temperature processing (e.g., melting techniques), not compatible with flexible substrates. Flexible perovskite-based X-ray detectors have been less explored but, in the last years, the number of reports on their feasibility is rapidly growing.^[35–37] The possibility of conforming ionizing radiation detectors and dosimeters onto a nonflat object is one of the primary desired features needed, for example, when detectors have to be integrated inside specific probes during radiation therapy,^[38] or in easy-wearable objects (e.g., bracelets and belt) and for potential vignetting limitation. Recently, Zhao et al.^[39] proposed a highly sensitive and flexible direct X-ray detector based on a porous nylon membrane with metal halide perovskite loaded by the infiltration method. Such a perovskite-filled membrane has good stability and high sensitivity to X-rays, comparable to those of perovskite single crystals. Excellent results were also presented by Demchyshyn et al.^[40] with an ultraflexible, conformable, and lightweight X-ray detector based on a photodiode architecture, able to stably operate in passive mode (at 0 V) with a sensitivity of $9.3 \mu\text{C Gy}^{-1} \text{cm}^{-2}$ and a limit of detection (LoD) of $0.58 \mu\text{G s}^{-1}$. Despite these remarkable detection performances, both these flexible devices, together with others in recent literature,^[41,42] envisage complex multilayered architectures and fabrication techniques requiring several steps and often oxygen-free environment.

Here we report on a novel approach for the implementation of a wearable and flexible X-ray detector, fully realized onto silk-satin and cotton fabrics. On the cotton fabric, poly(3,4-ethylenedioxythiophene):polystyrene sulfonate (PEDOT:PSS) patterns are screen-printed to realize the conductive electrodes of the device. The silk-satin fabric is employed not as a mere substrate, but it is functionalized to become the photoactive layer of the detector (directly absorbing the X-rays), by growing lead halide perovskite crystals directly embedded within the textile. The good detection performance, like sensitivity up to $(12.2 \pm 0.6) \mu\text{C Gy}^{-1} \text{cm}^{-2}$ and limit of detection ($3 \mu\text{Gy s}^{-1}$), low operating voltage (≤ 10 V), and operational stability, coupled with comfortability, breathability, and scalability, assess the potential of this new concept of fully textile X-ray detectors (TX-RD). Perovskite nanocrystals, polycrystals, or thin films have been recently proposed for textile photovoltaic applications, such as fiber-shaped perovskite solar cells around Ti wires,^[43,44] carbon nanotubes,^[45] or stainless steel (SS) wires^[46] that may be woven into electronic textile for energy harvesting applications. Perovskite solar cells adopting planar heterojunction configuration were integrated onto textile by Jung et al.^[30] and Lam et al.,^[47] but in these works the fabric represented only a support for the device bottom-up fabrication.

Indeed, here we present an innovative strategy to realize perovskite-based textile devices by feasibly growing perovskite crystals within silk-satin fabric, representing thus an effective active component of the device's architecture. This fabrication method involves screen-printed electrodes and drop-cast active layer, sewn together by conductive fibers, which provide the electrical connections, i.e., technologies which can be easily implemented in textile industry processes. It has to be noticed that the presence of lead, whose toxicity is severe to human health and impacting adversely on the environment,

has been considered since the beginning of the development of perovskite-based technology as the main issue against its large-scale deployment.^[48,49] The health hazard of lead is related to its entering in the bloodstream through ingestion or inhalation, but also through dermal contact. The design of a wearable device based on lead halide perovskite, i.e., potentially in direct contact with the human skin, must envisage thus a strategy to mitigate such an issue. In the case of the here-reported fully textile X-ray detectors, the perovskite-functionalized textile acting as absorbing layer is sandwiched between the two textiles with the screen-printed electrodes. Therefore, the perovskite would not enter in direct contact with the skin of the user. The employment of natural fabrics assures the sustainability and recyclability of the here-presented X-ray detectors.

Finally, the proof of concept of a large-area TX-RD matrix, characterized by a facile fabrication approach, is provided, paving the way to the development of a fully textile pixelated ionizing radiation detection system, which would represent an innovative and unique wearable item to map the dose received by an extended area exposed to the radiation, e.g., worn by patients during medical radiologic diagnostics and therapy treatments.

2. Results and Discussion

2.1. Material Characterization

The realization of the TX-RD consists of three different and straightforward steps carried out at room temperature and under ambient conditions: i) fabrication of textile electrodes, ii) growth from solution of perovskite crystals into textile substrates, iii) sew and assembly of the fabrics in the final and desired geometry. We present two different structures (planar: two-layer structures; and stacked: three-layer structures) which allow us to tune the layout of the fully textile X-ray detectors, adapting it to the specifications of the foreseen application. We also present a proof of concept of a sensing matrix based on stacked TX-RD devices.

Textile conductive electrodes are realized by a conductive polymer ink, PEDOT:PSS, screen-printed on cotton fabric. The resistance variation over a period of 5 months of the so-fabricated textile electrode is shown in Figure S1 (Supporting Information). The final electrode dimension depends on the prototype desired (stacked structure, matrix configuration, or planar device), and a simple ad-hoc serigraphic frame has been realized to match the specifications (Figure 1a). A conductive stainless steel thread, sewn directly onto the electrode fabric by means of a sewing machine, provides the electrical connections. The conductive thread has a linear resistance of $0.1 \Omega \text{cm}^{-1}$, and it is easily sewn along with the fabric to bring the electronic read-out system to the most comfortable place. The optical image of the cotton substrate is shown in Figure 1b, while the conductive cotton fabric constituting the electrodes with the typical bluish color PEDOT:PSS is reported in Figure 1c.

Such screen-printed conductive electrodes represent a flexible, durable, and deformable alternative to a standard metallic contact in wearable application. The sensing layer of the detector consists of a silk-satin fabric functionalized with perovskite

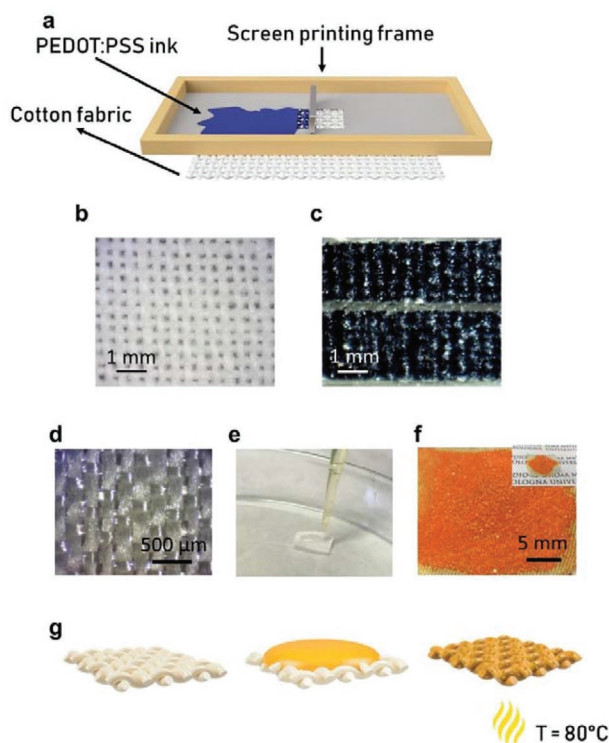


Figure 1. Substrates' modification. a) Schematic representation of the screen-printing procedure of the cotton conductive electrodes. b) Optical image of the cotton fabric. c) Top view of cotton fabric functionalized with PEDOT:PSS as textile electrodes. d) Optical picture of the top-side of the silk-satin fabric. e) Drop-cast deposition of MAPbBr₃ precursor solution on textile. f) Optical image of the silk-satin fabric fully covered with the embedded polycrystalline absorption layer. g) Sketch of the crystal deposition procedure on the textile.

crystals (Figure 1d–f). A volume of 100 mL every cm² of synthesized precursor solution of lead(II) bromide (PbBr₂) and methylammonium bromide (MABr) in *N,N* dimethylformamide (DMF) is drop-cast onto the fabric and let dry at 80 °C to uniformly grow perovskite crystals (Figure 1e).

Figure 1f shows a picture of the silk-satin fabric after the perovskite crystals' growth, showing the typical orange color of MAPbBr₃ crystals. To the best of our knowledge, this is the first example of a fast, low-cost, and uniform perovskite crystal growing procedure onto a fabric substrate. Thanks to typical satin weaving features, i.e., wrinkle-resistant, slipper, and tight stitches, the crystals cover the fabric uniformly and with a high density.

The deposition method here used allows us to achieve uniform active layers that exhibit crystals with a typical surface area of about (300 × 200) μm² and a thickness of about 50 μm. **Figure 2a** displays the optical image of the surface of the silk-satin fabric after the first step of functionalization with MAPbBr₃ crystals and a zoomed picture in the inset. Scanning electron microscope (SEM) images (Figure 2b,c; Figure S2, Supporting Information) show the tight binding and the intimate contact between perovskite crystals and the fabric, a crucial feature to envisage wearable applications for TX-RD devices directly integrated on garments and able to withstand wearing stresses. The energy-dispersive X-ray spectroscopy (EDX) image

in Figure 2d reports the distribution of crystals on the fabric after the first deposition step and their composition; the Br and Pb atoms, highlighted in green and red, respectively, are significantly present only in crystals, leaving the surrounding textile fibers lead and bromine free.

The crystallinity of perovskite crystals embedded into the final functionalized silk-satin fabric has been assessed by acquiring the X-ray diffraction (XRD) spectrum shown in Figure 2e. The diffraction peaks positioned at 15.1°, 30.2°, and 46.0° were converted into interplanar spacings, which correspond to (001), (002), and (003) crystal planes, respectively.^[50] The high peak intensity clearly indicates the high crystallinity nature of the sample with a constant orientation of (001) crystal planes parallel to the surface. This confirms that the drop-cast deposition process grants high quality and uniformly distributed crystals. Figure 2e also shows the spectrum of the same sample after 6 months of storage in air and dark conditions. The characteristic diffraction peaks resulted unchanged, indicating that crystalline structure is not affected by the aging. However, some additional XRD peaks can be noticed, at 21.1°, 33.7°, 37.1°, 43.1°, and 48.5° (2θ). From the comparison with literature we can identify them to those characteristics of MAPbBr₃ powder.^[51,52]

In order to achieve a TX-RD able to efficiently collect the charges induced by the interaction of the active layer with the X-rays, it is fundamental to enhance the radiation absorption by increasing the uniformity and the thickness of the active layer. Therefore, the active layers' deposition consists in three consecutive drop-cast steps alternated with a proper annealing procedure. After each deposition, the numbers and the crystals' arrangement change from single and isolated crystals to a uniform surface coverage. The crystals' tight and dense arrangement transforms the silk-satin substrate into an effective photoactive textile (**Figure 3a**) and creates a continuous and thick (300 μm on the average) path that can efficiently transport charge carriers. The XRD spectrum of the perovskite active layer on silk-satin fabric after three steps of drop-cast deposition is reported in Figure S3 (Supporting Information), showing the same orientation of crystal planes as the spectrum shown in Figure 3e for one-step deposited perovskite. The inset in Figure 3a highlights the Br (green) and Pb (red) uniform dispersion through the entire crystalline layer. In the same vein, Figure 3b shows a SEM image of the uniform and dense PEDOT:PSS coating of the cotton fabric, while the inset underlines through EDX analysis the homogeneous distribution of sulfur (red), which characterizes the PEDOT:PSS presence.

Photoluminescence (PL) spectroscopy measurements of the perovskite-loaded silk-satin textile assess that the optical properties of the perovskite layer grown onto the fabric are in line with the ones reported for free-standing MAPbBr₃ single crystals,^[53] thus confirming the crystallinity of the perovskite functionalized satin fabric. Figure S4 (Supporting Information) shows the spectra acquired under a 375 nm coherent light from a 5 nW laser, for three different angles between the functionalized fabric and the incident laser direction. In our case, for high values of this angle, the PL spectrum presents two peaks at 540 and 574 nm, corresponding to the PL emitted and light transmitted, respectively. The presence of two distinct peaks with different relative intensities can be interpreted referring

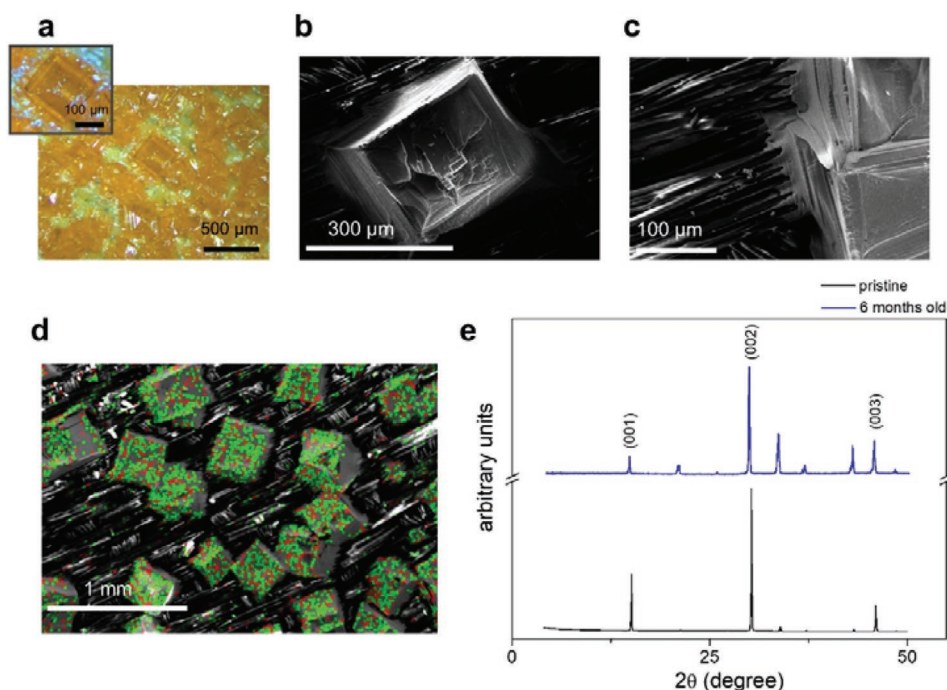


Figure 2. Optical and structural characterization. a) Optical image of MAPbBr₃ crystals. b) Top-view SEM image of one MAPbBr₃ single crystal. c) SEM image of a MAPbBr₃ crystal embedded in the silk-satin fabric. d) Top-view SEM image of the silk-satin fabric after the first deposition step, showing the distribution of crystals embedded into the fabric. Red and green dots highlight the presence of lead and bromine, respectively. e) XRD spectrum of MAPbBr₃ crystals embedded into the silk-satin fabric. The peaks correspond to the (001), (002), and (003) crystal planes. The blue spectra are acquired 6 months later.

to the results reported by Wenger et al.,^[53] who showed that a MAPbBr₃ single crystal PL spectrum is affected by an energy redshift between the emitted and transmitted peaks acquired changing the relative position between light source, sample, and detector.

2.2. Detector Characterization

Since both the electrodes and the photoactive layer are textile based, the stacked configuration is realized by sewing them together, as shown in Figure 3c,d, to obtain an intimate and stable electric contact. The sensor dimension depends on the areas of the conductive electrodes and of the functionalized silk-satin fabric. We realized TX-RD sensors with different areas from 0.06 up to 1 cm². The schematic of the assembly is displayed in Figure 3d.

The absorption of hard X-rays (40–150 kVp) by silk-satin and cotton fabrics and by PEDOT:PSS is much lower than that of MAPbBr₃ crystals due to their organic nature (composed by low Z atoms), as shown in Figure S5 (Supporting Information), which reports the attenuated fraction as a function of thickness for all the materials present in the TD-XR device. The perovskite functionalized silk-satin fabric absorbs ≈100% X-ray photons at 40 kVp (15 keV mean energy) and the negligible absorption of the cotton fabric and PEDOT:PSS allows us to fully exploit the absorption of the perovskite-loaded textile layer without having to take into account shielding effects due to the top layers of the device in the stacked architecture.

Typical current–voltage (*I*–*V*) characteristics in the dark of a stacked TX-RD device show a limited hysteresis as well as good Ohmic behavior, for an applied voltage from –5 to +5 V (Figure 4a). The average dark bulk resistance is (1.8 ± 0.9) GΩ measured over eight samples. The bulk resistance is calculated considering the value extracted from the linear fit of the *I*–*V* curves, both increasing and decreasing the bias sweep. It is worth remembering that, apart from the annealing process (at 80 °C), all the procedures, starting from the precursor solution processing, deposition, assembling, characterization, and storage, have been done in air under environmental conditions. The textile devices' performance as an X-ray detector was tested in air without encapsulation.

Figure 4b shows the TX-RD photocurrent real-time response under irradiation with high-energy photons delivered at 150 kVp, changing the anodic current in the range of 100–500 μA to deliver four different dose rates from 1.5 to 6.4 mGy s⁻¹. This plot is realized by the subtraction of the average dark current to each measured current value (*I*_i – *I*_{dark}). The X-ray beam intermittently reaches the tested sample alternating 5 s of irradiation and 5 s of dark by a mechanical lead shutter. Multiple subsequent on/off cycles at the same dose rate were acquired to estimate the average photocurrent generated, defined as the difference between the average current value under X-rays and the average dark current before switching the X-ray beam on. The sample was biased at 5 V during the measurements (electric field of about 0.017 V μm⁻¹, calculated as the ratio between the bias and the spacing between PEDOT:PSS electrodes, estimated

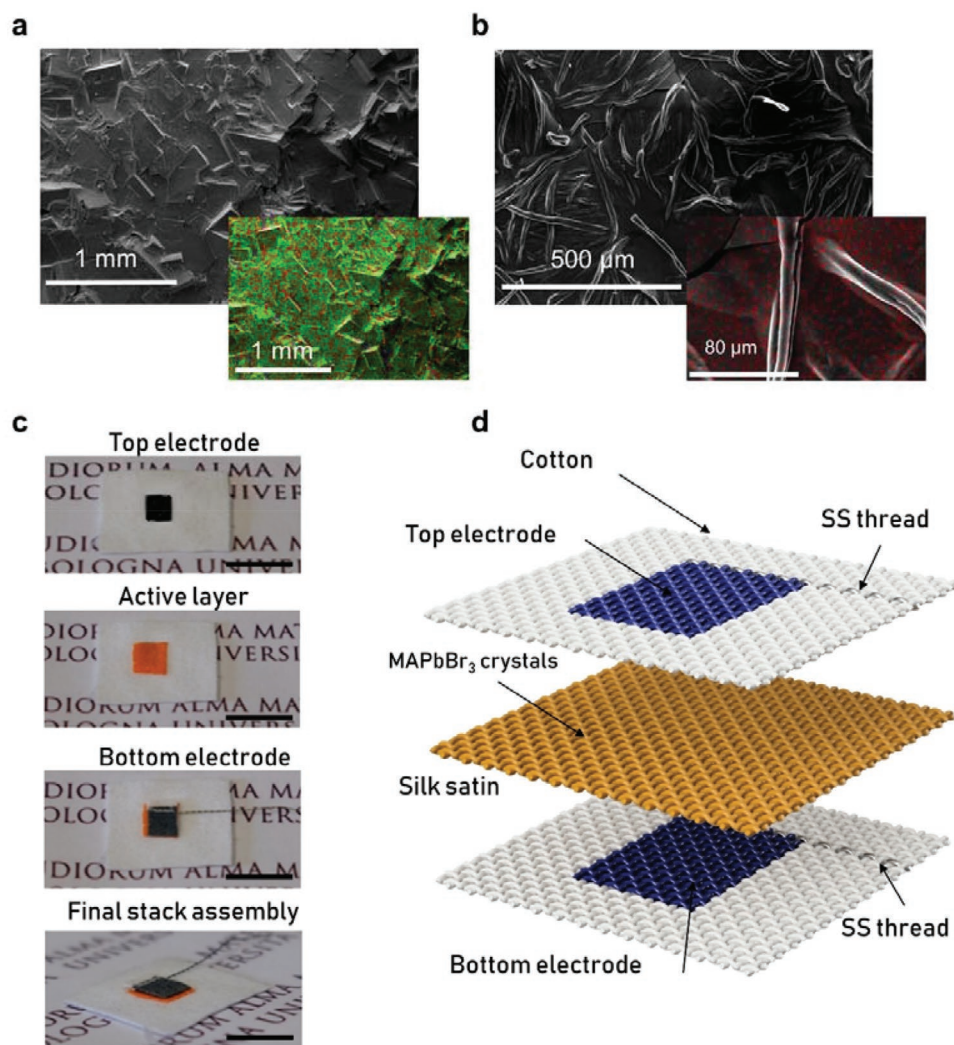


Figure 3. TD-RX stacked devices. a) SEM and EDX (inset) of the MAPbBr₃ absorption layer after three subsequent drop-cast depositions. b) SEM image showing the uniformity of the screen-printed PEDOT:PSS layer on cotton. Top-view EDX image (inset) showing the homogeneous distribution of sulfur (red dots), the identifying element of PEDOT:PSS. c) Fabrication step of the TX-RD stacked devices. The three layers are sewn together. Black scale bar is 1 cm. d) Schematics of the stacked TX-RD, highlighting the presence of stainless steel (SS) conductive thread.

about 300 μm in both planar and stacked geometry), to meet the low-power consumption request of wearable devices. Figure 4c shows the TX-RD stability when irradiated with 15 subsequent irradiation cycles at a high dose rate of 8.0 mGy s^{-1} . The response is sharp, fast, and repeatable over multiple cycles with a relative variation of the photocurrent lower than 3%. Furthermore, we performed a crumpling test to better assess the good connection ensured by deposition and the sewing procedure. It consists in wrinkling the fabric (see Figure S6a in the Supporting Information) multiple times and measuring the sensors photocurrent before and after 20 repeated wrinkling. Figure S6b (Supporting Information) shows the response when the sample is irradiated with 40 and 150 kVp X-ray beams. After 20 wrinkling, the measured photocurrent decreases less than 30%. This indicates that the application of severe stress can just slightly decrease the response without making the device unusable.

The detector's X-ray-induced photocurrent density (normalized by the device area) exhibits a linear trend with the incident dose with bias values of 5 and of 10 V applied to the sample. The slope of the X-ray photocurrent density versus the dose rate curve is defined as the sensitivity per unit area of the sample (Figure 4d). The sensitivity at 5 V in the stacked configuration reaches the value of $(5.7 \pm 0.9) \mu\text{C Gy}^{-1} \text{cm}^{-2}$ at 150 kVp, and a top value of $(12.2 \pm 0.6) \mu\text{C Gy}^{-1} \text{cm}^{-2}$ applying a bias of 10 V, corresponding to an applied electric field of $0.033 \text{ V } \mu\text{m}^{-1}$. These values are in line with those recently reported for flexible perovskite detectors realized onto plastic substrates with complex heterostructure architectures and with multistep fabrication processes in controlled conditions such as nitrogen atmosphere.^[37,40]

The here-reported TX-RDs are instead realized in air by low-tech deposition process with a simple device architecture, easily replicable employing standard printing technologies for textiles. The top sensitivity recorded well compares with the one of state-of-the-art inorganic materials currently used to fabricate

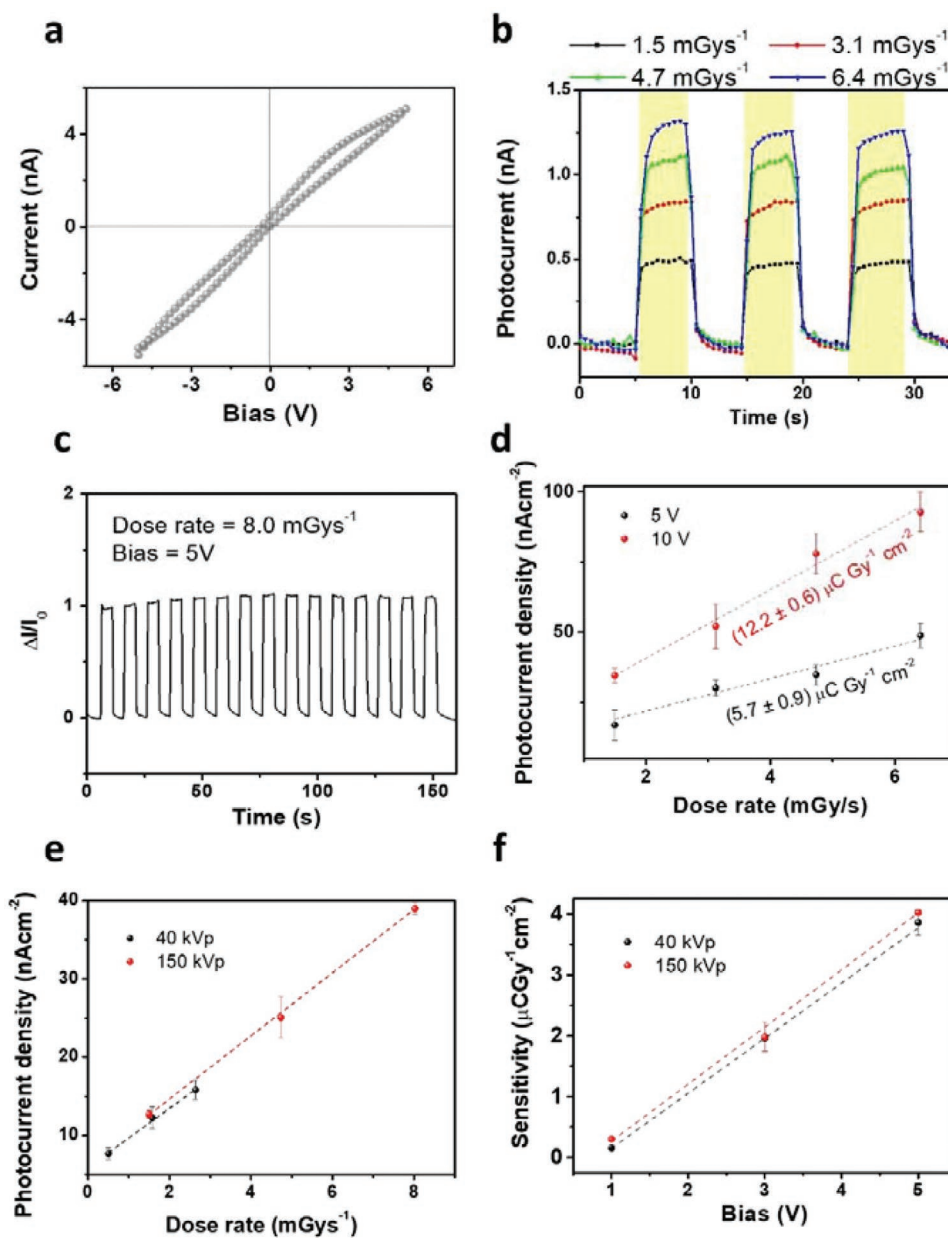


Figure 4. Response of TX-RD in stacked configuration. a) Typical current–voltage characteristics of the device in dark condition, showing relatively low hysteresis of the device. b) Dynamic detector response of a stacked TX-RD biased at 5 V, under X-ray beam (150 kVp, 47.4 keV mean energy of the spectrum) at different incident dose rates. The yellow boxes indicate the time window when the X-ray beam is turned on (5 s ON and 5 s OFF). c) Reproducibility of photocurrent dynamic response, normalized by its initial value, over 15 X-ray irradiation cycles (5 s ON and 5 s OFF each) at 8 mGy s⁻¹. The sample was polarized with a constant bias of 5 V during the entire measurement. d) X-ray induced photocurrent as a function of the incident radiation dose rate for two different biases: 5 and 10 V, and e) different accelerating voltages of the X-ray tube: 40 and 150 kVp. The linearity of the response with the dose rate is shown for each data set. f) Linear scaling with the bias of the sensitivity to X-rays recorded under 40 and 150 kVp X-ray beam irradiation.

large-area detectors (amorphous selenium has a typical value of 25 $\mu\text{C Gy}^{-1} \text{cm}^{-2}$ at 10 V μm^{-1} for 200 μm thick active layer typically).^[54]

Figure 4e reports the TX-RD response recorded under X-rays of 40 and 150 kVp at different dose rates for a constant bias of 5 V (mean value and standard deviation over three subsequent irradiation cycles). The linear response with the increasing dose rate is assessed both at 150 and 40 kVp, demonstrating the

capability of the TX-RD to be used as real-time direct dosimeters under a wide range of X-ray energies and dose rates, from 500 $\mu\text{Gy s}^{-1}$ up to 8.0 mGy s⁻¹. The sensitivity value linearly increases with the increasing value of the applied bias (from 1 to 5 V in Figure 4f) and, interestingly enough, it shows a scant dependence on the X-ray beam energy (see also Figure S7 in the Supporting Information), opening to the potential application for energy-independent dosimetry. The detectors' performances

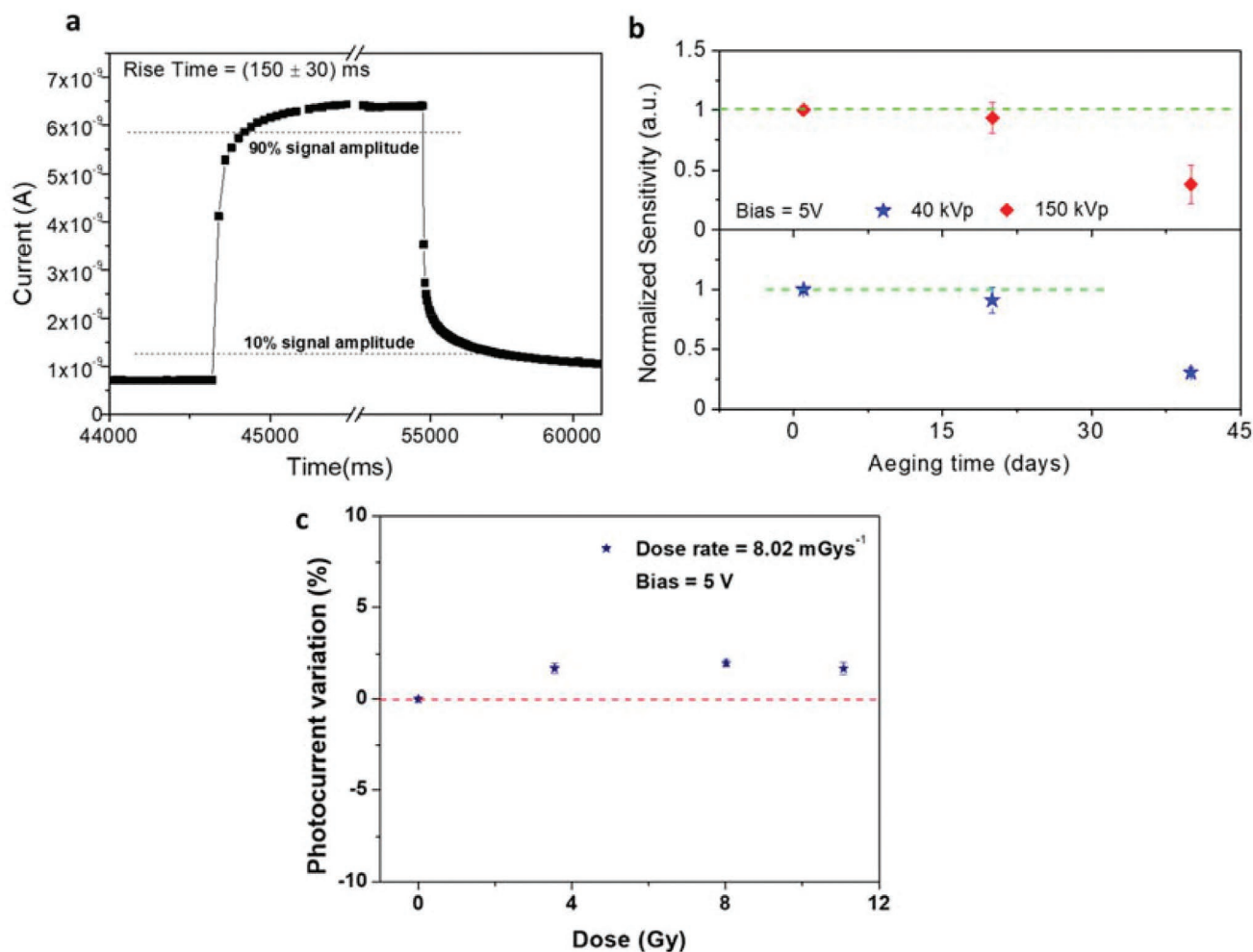


Figure 5. a) Single X-ray pulse at a bias of 5 V and 8 mGy s^{-1} . Rise time is defined as the time for the signal to rise from 10% to 90% of its steady-state value. b) Ageing test of the textile X-ray detector performed over 40 days. c) Photocurrent variation recorded after prolonged exposure to 150 kVp X-ray beam. The photocurrent response was measured with an X-ray dose rate of 8 mGy s^{-1} impinging on the device.

at 1 V are reported in Figure S8 (Supporting Information). The development of a textile electronic device imposes to envisage low-bias operation in order to be battery operating, portable, lightweight, low cost, even disposable, and with reduced electric risk for the user. Further, metal halide perovskites are well known to suffer from instability due to electric-field-induced ion migration^[55] and low-voltage operation must be preferred to mitigate this issue.

The response time of the detector, calculated as the time for the signal to rise from 10% to 90% of its steady-state value, resulted in (150 ± 30) ms, at 5 V bias under 8 mGy s^{-1} X-ray irradiation, as shown in Figure 5a.

The device performance under 150 and 40 kVp X-ray beam irradiations with an applied potential of 5 V has been monitored for 40 days (Figure 5b). During the first 20 days, the device sensitivity loses less than 10% of its initial value while after more than 1 month the sensitivity value decreased more than 50%. As a further test of the operational device stability without encapsulation, we tested the radiation hardness of our devices 15 days after fabrication. The device was biased

at 5 V and irradiated with a constant X-rays dose rate of 8 mGy s^{-1} .

Figure 5c reports the photocurrent variation acquired after prolonged exposure of the device to X-rays. The photocurrent has been measured after each step of irradiation. A variation within the 1% of the photocurrent signal with respect to the starting value was recorded up to a total delivered dose of 11.1 Gy. This total amount is equivalent to about 105 times the dose typically delivered in X-ray chest radiography.^[56]

In addition, we performed bending tests comparing the signals acquired in a flat sample and in a bending position. Bending the sample down to a radius of 8 mm, compatible with most of the wearable applications, both the photocurrent and the sensitivity increase (Figure S9a,b, Supporting Information). The photocurrent increases about three times. Accordingly, the sensitivity increases from (1.2 ± 0.1) to $(6.5 \pm 0.1) \mu\text{C Gy}^{-1} \text{ cm}^{-2}$. This phenomenon can be correlated to a tighter contact between the textile layers, allowing a more efficient charge collection.

Taking advantage of the easy material deposition processes and device customization, TX-RD devices with planar

architecture were fabricated using one layer of cotton fabric functionalized as conductive electrode textile and a silk-satin fabric functionalized as a photoactive layer. Perovskite crystals have been grown embedded into the silk-satin fabric, as for the stacked configuration, while two parallel PEDOT:PSS-based conductive strips were screen-printed on the cotton fabric. The average spacing between the electrodes is $(330 \pm 10) \mu\text{m}$. The photoactive silk-satin fabric was sewn onto the cotton electrode, and stainless steel thread connections ensure electric contact with the read-out system. Figure S10a (Supporting Information) shows the schematic representation of the planar TX-RD geometry. Other configurations can be explored according to the targeted application, e.g., the geometry of the electrodes can be easily changed in interdigitated electrodes, as shown in Figure S10b (Supporting Information). This can preserve detection performance in terms of photocurrent density, linear response with increasing dose rate, and the corresponding sensitivity $(4.5 \pm 0.2) \mu\text{C Gy}^{-1} \text{cm}^{-2}$ at 5 V, as confirmed by the measurements of the photocurrent density versus dose rate reported in Figure S10c (Supporting Information). This sensitivity value is also in line with that recorded for the stacked configuration (Figure 4d).

An important figure of merit to characterize the detector's performance is the minimum detectable dose, namely the LoD,

defined as the minimum intensity of X-rays which provides a signal-to-noise ratio (SNR) equal to 3 (International Union of Pure and Applied Chemistry standard definition^[57]). Figure S11 (Supporting Information) reports the SNR over three orders of magnitude of dose rates for both stacked and planar configurations. Major details about the LoD calculation can be found in the Supporting Information. The graphically extracted LoD is comparable for the two architectures, i.e., $3 \mu\text{Gy s}^{-1}$ for the stacked and $8 \mu\text{Gy s}^{-1}$ for the planar configuration, at the same device characterization condition (bias 5 V and X-rays accelerating voltage of 150 kVp). These values are well compatible with the typical radiation doses used in most medical diagnostic and dosimetry applications.^[58–60] A detailed comparison of the detection performance of the TD-RX device with the state-of-the-art flexible perovskite-based X-ray detectors is reported in Figure S12 (Supporting Information).

Thanks to the possibility of easily screen-print different electrode patterns with a sub-millimeter resolution, we also developed a pixelated X-ray sensor matrix. The sensor matrix consists of nine independent pixels, defined by the intersection of three electrodes printed both on the top and the bottom fabric, as shown in the schematic of Figure 6a. The photoactive textile, functionalized with perovskite crystals, is sandwiched between them. Figure 6b and Figure 6c report the normalized dark current and photocurrent for each of the 9 pixels,

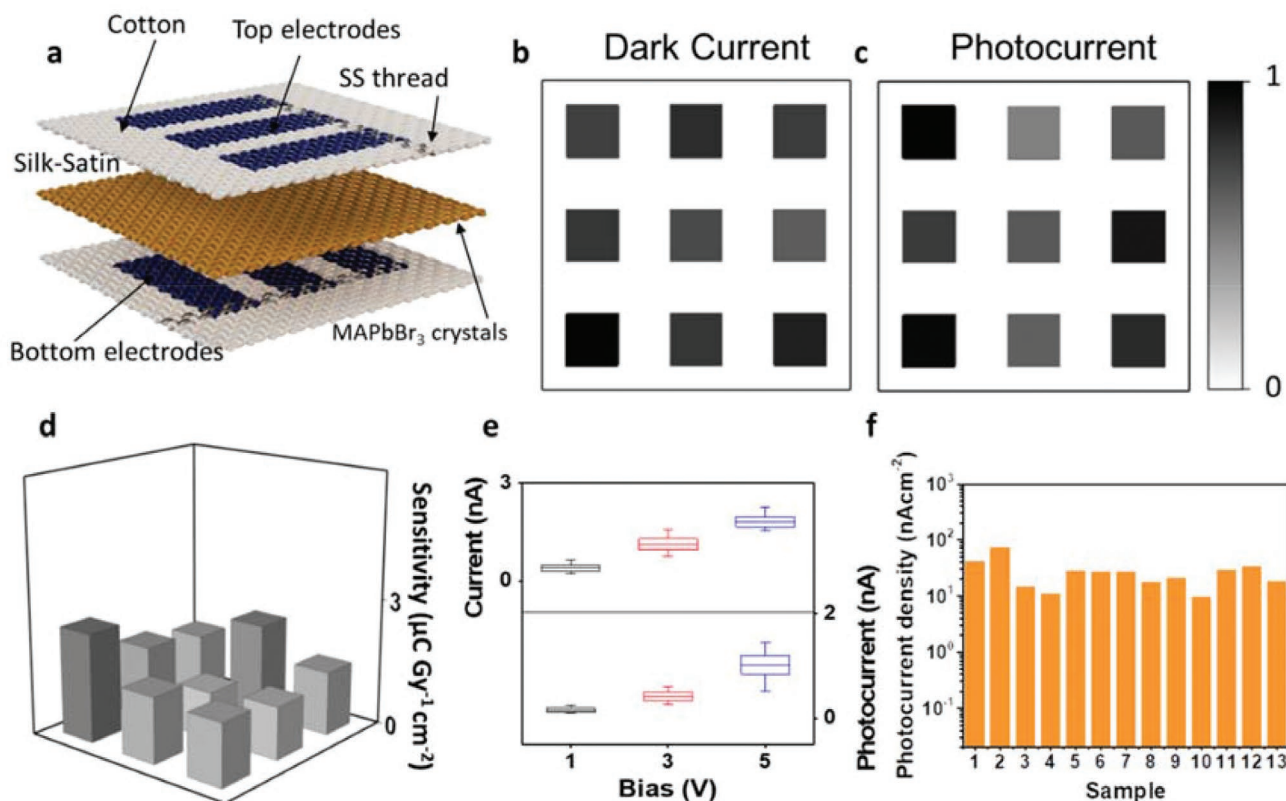


Figure 6. Pixel matrix TX-RD. a) Schematic of the assembly of the textile matrix sensor. Each pixel is identified by the intersection of PEDOT:PSS electrodes printed both on the top and bottom fabrics. In the middle, there is the perovskite-functionalized fabric acting as the absorbing layer. The three fabrics are sewn together reaching the final device layout. Distribution of the b) normalized dark current and c) X-ray-induced photocurrent (bias 5 V—dose rate 8.0 mGy s^{-1}) for each of the 9 pixels. d) Sensitivity per unit area of all the pixels when 5 V is applied with an impinging X-ray beam at 150 kVp. The plot of the average X-ray photocurrent of the sensor matrix as a function of the dose rate is reported in the inset. e) Statistical distribution over two matrix TX-RD samples of the dark current and photocurrent response for three different bias (below 5 V) at a dose rate of 8 mGy s^{-1} . f) Photocurrent signal amplitude acquired by 13 TX-RD operated with a bias of 5 V and irradiated with high-energy photons' flux delivered by a 150 kVp X-ray source.

respectively. The recorded variability of 13% for the dark current and of 20% for the acquired photocurrent signal highlights the overall homogeneity of sensors' response. To better stress this aspect, Figure 6d reports the sensitivity per unit area of each pixel at 5 V under an impinging X-ray beam at 150 kVp. The average sensitivity per unit area is $(1.9 \pm 0.3) \mu\text{C Gy}^{-1} \text{cm}^{-2}$. The TX-RD reproducibility in matrix configuration was assessed realizing two matrices and recording their dark current and the X-ray photocurrent response.

Figure 6e reports their statistic distribution in a box chart plot, showing also their linear increase with increasing applied voltage. The high tested dose rate of 8.0 mGy s^{-1} assesses the reliability of the sensor matrix operation under strong irradiation conditions.

The variation of X-ray photocurrent density signal acquired from 13 different TX-RDs, both in single and matrix stacked configurations at the same operation conditions, is reported in Figure 6f.

3. Conclusion

In this work, we report on the novel realization and characterization of a fully textile real-time and direct X-ray detector (TX-RD). This device is realized by sewing together differently functionalized fabrics: cotton fabrics with screen-printed PEDOT:PSS patterns act as electrodes; silk-satin fabric embedded with perovskite crystals acts as the photoactive layer of the detector absorbing the X-ray radiation. The response to X-rays has been assessed to scale linearly with increasing dose rates and be stable for a wide range of X-ray energies (40–150 kVp) and dose rates (from $500 \mu\text{Gy s}^{-1}$ up to 8.0 mGy s^{-1}). The best sensitivity obtained by this new class of textile detectors is $12.2 \pm 0.6 \mu\text{C Gy}^{-1} \text{cm}^{-2}$, and an LoD down to $3 \mu\text{Gy s}^{-1}$ has been estimated from experimental data. The low operating bias (down to 1 V), stable response over a period of 20 days, coupled with good flexibility and bendability behavior, demonstrates the applicability of the here-reported TX-RD as wearable devices. Two device geometries (stacked and planar) are reported with comparable performances, paving the way for further innovative device architecture developments. The planar configuration allows us to easily enlarge the active area of the device exploiting interdigitated electrode geometry without affecting the detection performance (thus enhancing the detector efficiency and total sensitivity). On the other hand, the stacked configuration allows a scale-up to a pixelated detector matrix, with good reproducibility among different pixels. A key and unique feature of the here-presented fully textile detectors is their low-cost and low-tech fabrication, exploiting standard printing technologies for textiles carried out in air atmosphere, a definite advancement with respect to the latest reported flexible perovskite-based X-ray detectors that employ complex heterostructure architectures fabricated through highly controlled multistep deposition processes. For the practical application of the here-proposed textile dosimeter, an aluminum foil packaging for storage and breathable but water-repellent textiles as coverage (e.g. Gore-Tex) of the device could be foreseen in order to envisage longer time stability. Finally, the employment of natural fabrics, such as silk-satin and cotton, represents an

added value in terms of biocompatibility, recyclability, comfort, and breathability for the effective application of this new class of textile sensors as wearable ionizing radiation dosimeters, which can be directly realized into smart garments.

4. Experimental Section

Materials: Clevis PH1000, ethylene glycol (EG), polyethylene glycol (PEG), PbBr_2 , $\text{CH}_3\text{NH}_3\text{Br}$, and dimethylformamide were purchased from Sigma–Aldrich. All the chemicals were used at their reagent grade without any further purification. The conductive textile thread made of stainless steel was purchased from Adafruit.

Device Fabrication: PEDOT:PSS textile electrodes were fabricated by using conventional serigraphy screen-printing technique applying custom masks onto the frame in order to impress the fabric with the desired geometry. Clevis PH1000 and EG were sonicated together for 15 min in a 95:5 volume ratio, and 10% w/w of PEG was successively added. The solution was stirred for 20 min to disperse the PEG completely. A more viscose conductive ink was realized by drying the liquid solution in an oven at 70°C for 1 h. The final conductive paste was placed onto the serigraphy frame and squeezed manually onto the cotton. To ensure the electrical contact with the read-out setup, a stainless steel conductive thread was sewn onto the electrode and along the fabric using an Elna Xplore 340 sewing machine. The precursor perovskite 1 M solution was realized by adding the PbBr_2 and MABr powder in a stoichiometric ratio of 1:1 in DMF solvent. It was vigorously mixed for 4 h and then filtered with a Teflon filter ($0.45 \mu\text{m}$ size) to remove colloids eventually present. The solution was stored at 4°C in the dark. The so-obtained solution was employed to deposit MAPbBr_3 single crystals onto silk-satin fabric. It was first washed in isopropanol to remove possible industrial residues. A piece of sizes in the range of 20–30 mm² was placed onto a Petri dish, and a typical amount of 100 mL cm^{-2} of perovskite solution was deposited by the drop-casting method. The fabric was then covered with a Petri dish to control and speed down the solvent's evaporation, and annealed at 80°C on a hot plate until all the solvent was evaporated. The deposition process was repeated three times in order to increase the crystals' density. The entire procedure occurred under a chemical fume hood at ambient conditions, avoiding direct light exposition to preserve the samples from photo-oxidation.

The as-prepared perovskite-functionalized fabric was used to realize a stacked textile X-ray detector, placing it between two conductive cotton fabrics and sewing all the textile layers together by a sewing machine, and a planar textile X-ray detector (facing the satin fabric, with crystals embedded into it, directly onto a cotton textile; the fabric electrode was composed of two PEDOT:PSS strips screen-printed by creating a channel of $300 \mu\text{m}$).

Finally, two cotton textiles, each with three parallel conductive strips, were employed as top and bottom electrodes in order to realize a large-area X-ray matrix sensor.

Morphology Characterization: The morphological features of the functionalized cotton and silk-satin textile with PEDOT:PSS and perovskite crystals were assessed both with optical and electron microscopes. An Optika microscope model SLK-5 with an HD Optika C-HE camera was used to acquire electrodes' and crystals' pictures. SEM (Cambridge Stereoscan 360) images were obtained to investigate the crystal structure, morphology, composition, and coating features of the cotton and silk-satin fabric. The accelerating voltage was 20 kV with a probe current of 4 pA. The same instrument, coupled with an energy-dispersive spectrometer, was used to perform the EDX to define the presence and distribution of the chemical elements in these samples.

The XRD spectrum on the perovskite crystal was acquired by employing a PANalytical X'Pert Pro automated diffractometer equipped with an X'celerator multielement solid-state detector. The diffractometer was operated in Bragg–Brentano $\theta/2\theta$ para-focusing geometry using Ni-filtered $\text{Cu K}\alpha$ radiation without monochromator in the diffracted beam.

An optical bench equipped with a Taiko PDL M1 high-end picosecond diode laser driver, an LDH-IB-375-B laser head by PicoQuant and a Thorlabs compact spectrometer CC S200, was used to perform the photoluminescence spectroscopy measures.

Device Characterization under X-Rays: Characterization under X-rays was performed using the broad X-ray spectrum provided by a Hamamatsu L12161 X-ray tube with the tungsten target at fixed 40 and 150 kVp operating voltages. W-target X-ray tube is reported in Figure S13 (Supporting Information). The filament current was changed between 100 and 500 μA leading to an incident dose rate on the samples between 500 and 2640 $\mu\text{Gy s}^{-1}$ (at 40 kVp) and between 1500 and 8000 $\mu\text{Gy s}^{-1}$ (at 150 kVp). The dose rate calibration was previously performed employing the Barracuda radiation detector (RTI Group). The modulation of the beam was obtained with a mechanical lead shutter placed close to the X-ray tube window. Keithley SMU 2614 was used in combination with a custom LabVIEW program for electrical signal acquisition. The measurements of the X-ray detection response under bending were performed by rolling the sample around rigid cylinders to provide quantitative evaluation of the bending radius.

Supporting Information

Supporting Information is available from the Wiley Online Library or from the author.

Acknowledgements

The authors acknowledge Prof. Luca Pasquini for providing the XRD measurements and fruitful discussion for its interpretation. The National Operation Program (PON) of the Ministry of Education, University and Research supported this work (Project PON-MIUR 2018 (Italy) ARS01_00996: "TEX-STYLE—Nuovi tessuti intelligenti e sostenibili multi-settoriali per design creativo e stile made-in-Italy").

Open Access Funding provided by Università degli Studi di Bologna within the CRUI-CARE Agreement.

Conflict of Interest

The authors declare no conflict of interest.

Data Availability Statement

The data that support the findings of this study are available from the corresponding author upon reasonable request.

Keywords

perovskite, textile sensors, wearable sensors, X-ray detectors

Received: September 9, 2021

Revised: March 11, 2022

Published online: April 14, 2022

- [1] A. Hatamie, S. Angizi, S. Kumar, C. M. Pandey, A. Simchi, M. Willander, B. D. Malhotra, *J. Electrochem. Soc.* **2020**, *167*, 037546.
 [2] G. M. N. Islam, A. Ali, S. Collie, *Cellulose* **2020**, *27*, 6103.
 [3] I. Gualandi, M. Tassarolo, F. Mariani, L. Possanzini, E. Scavetta, B. Fraboni, *Polymers* **2021**, *13*, 894.

- [4] I. Del Agua, D. Mantione, U. Ismailov, A. Sanchez-Sanchez, N. Aramburu, G. G. Malliaras, D. Mecerreyes, E. Ismailova, *Adv. Mater. Technol.* **2018**, *3*, 1700322.
 [5] F. Mariani, M. Serafini, I. Gualandi, D. Arcangeli, F. Decataldo, L. Possanzini, M. Tassarolo, D. Tonelli, B. Fraboni, E. Scavetta, *ACS Sens.* **2021**, *6*, 2366.
 [6] G. B. Tseghai, B. Malengier, K. A. Fante, A. B. Nigusse, B. B. Etana, L. Van Langenhove, in *2020 IEEE Int. Conf. on Flexible and Printable Sensors and Systems (FLEPS)*, IEEE, Piscataway, NJ **2020**, pp. 1–4.
 [7] D. Pani, A. Dessi, J. F. Saenz-Cogollo, G. Barabino, B. Fraboni, A. Bonfiglio, *IEEE Trans. Biomed. Eng.* **2016**, *63*, 540.
 [8] E. Bihar, T. Roberts, E. Ismailova, M. Saadaoui, M. Isik, A. Sanchez-Sanchez, D. Mecerreyes, T. Hervé, J. B. De Graaf, G. G. Malliaras, *Adv. Mater. Technol.* **2017**, *2*, 1600251.
 [9] M. D. Husain, R. Kennon, T. Dias, *J. Ind. Text.* **2014**, *44*, 398.
 [10] L. Possanzini, M. Tassarolo, L. Mazzocchetti, E. G. Campari, B. Fraboni, *Sensors* **2019**, *19*, 4686.
 [11] G. B. Tseghai, B. Malengier, K. A. Fante, L. V. Langenhove, *Proceedings* **2021**, *68*, 1.
 [12] F. Mariani, I. Gualandi, D. Tonelli, F. Decataldo, L. Possanzini, B. Fraboni, E. Scavetta, *Electrochem. Commun.* **2020**, *116*, 106763.
 [13] L. Possanzini, F. Decataldo, F. Mariani, I. Gualandi, M. Tassarolo, E. Scavetta, B. Fraboni, *Sci. Rep.* **2020**, *10*, 17180.
 [14] L. Wang, L. Wang, Y. Zhang, J. Pan, S. Li, X. Sun, B. Zhang, H. Peng, *Adv. Funct. Mater.* **2018**, *28*, 1804456.
 [15] H. Hardianto, B. Malengier, G. De Mey, L. Van Langenhove, C. Hertleer, *J. Eng. Fibers Fabr.* **2019**, *14*.
 [16] A. Lund, Y. Tian, S. Darabi, C. Müller, *J. Power Sources* **2020**, *480*, 228836.
 [17] Z. Zhao, Q. Huang, C. Yan, Y. Liu, X. Zeng, X. Wei, Y. Hu, Z. Zheng, *Nano Energy* **2020**, *70*, 104528.
 [18] I. Jeerapan, J. R. Sempionatto, A. Pavinatto, J.-M. You, J. Wang, *J. Mater. Chem. A* **2016**, *4*, 18342.
 [19] J. Lv, I. Jeerapan, F. Tehrani, L. Yin, C. A. Silva-Lopez, J.-H. Jang, D. Joshua, R. Shah, Y. Liang, L. Xie, F. Soto, C. Chen, E. Karshalev, C. Kong, Z. Yang, J. Wang, *Energy Environ. Sci.* **2018**, *11*, 3431.
 [20] I. Nuramdhani, M. Jose, P. Samyn, P. Adriaenssens, B. Malengier, W. Deferme, G. De Mey, L. Van Langenhove, *Polymers* **2019**, *11*, 345.
 [21] A. Ciavatti, L. Basiricò, I. Fratelli, S. Lai, P. Cosseddu, A. Bonfiglio, J. E. Anthony, B. Fraboni, *Adv. Funct. Mater.* **2019**, *29*, 1806119.
 [22] H. M. Thirimanne, K. D. G. I. Jayawardena, A. J. Parnell, R. M. I. Bandara, A. Karalasingam, S. Pani, J. E. Huerdler, D. G. Lidzey, S. F. Tedde, A. Nisbet, C. A. Mills, S. R. P. Silva, *Nat. Commun.* **2018**, *9*, 2926.
 [23] M. J. Griffith, S. Cottam, J. Stamenkovic, J. A. Posar, M. Petasecca, *Front. Phys.* **2020**, *8*, 22.
 [24] L. Basiricò, A. Ciavatti, B. Fraboni, *Adv. Mater. Technol.* **2021**, *6*, 2000475.
 [25] Z. Li, F. Zhou, H. Yao, Z. Ci, Z. Yang, Z. Jin, *Mater. Today* **2021**, *48*, 155.
 [26] H. Wei, J. Huang, *Nat. Commun.* **2019**, *10*, 1066.
 [27] M. Kaltenbrunner, M. S. White, E. D. Głowacki, T. Sekitani, T. Someya, N. S. Sariciftci, S. Bauer, *Nat. Commun.* **2012**, *3*, 770.
 [28] M. Kaltenbrunner, G. Adam, E. D. Głowacki, M. Drack, R. Schwödiauer, L. Leonat, D. H. Apaydin, H. Groiss, M. C. Scharber, M. S. White, N. S. Sariciftci, S. Bauer, *Nat. Mater.* **2015**, *14*, 1032.
 [29] M. Tassarolo, I. Gualandi, B. Fraboni, *Adv. Mater. Technol.* **2018**, *3*, 1700310.
 [30] J. W. Jung, J. H. Bae, J. H. Ko, W. Lee, *J. Power Sources* **2018**, *402*, 327.
 [31] L. Basiricò, A. Ciavatti, I. Fratelli, D. Dreossi, G. Tromba, S. Lai, P. Cosseddu, A. Bonfiglio, F. Mariotti, C. Dalla Val, V. Bellucci, J. E. Anthony, B. Fraboni, *Front. Phys.* **2020**, *8*, 13.
 [32] L. Basiricò, S. P. Senanayak, A. Ciavatti, M. Abdi-Jalebi, B. Fraboni, H. Sirringhaus, *Adv. Funct. Mater.* **2019**, *29*, 1902346.

- [33] S. Yakunin, D. N. Dirin, Y. Shynkarenko, V. Morad, I. Cherniukh, O. Nazarenko, D. Kreil, T. Nauser, M. V. Kovalenko, *Nat. Photonics* **2016**, *10*, 585.
- [34] H. Wei, Y. Fang, P. Mulligan, W. Chuirazzi, H.-H. Fang, C. Wang, B. R. Ecker, Y. Gao, M. A. Loi, L. Cao, J. Huang, *Nat. Photonics* **2016**, *10*, 333.
- [35] J. Liu, B. Shabbir, C. Wang, T. Wan, Q. Ou, P. Yu, A. Tadich, X. Jiao, D. Chu, D. Qi, D. Li, R. Kan, Y. Huang, Y. Dong, J. Jasieniak, Y. Zhang, Q. Bao, *Adv. Mater.* **2019**, *31*, 1901644.
- [36] A. Ciavatti, R. Sorrentino, L. Basiricò, B. Passarella, M. Caironi, A. Petrozza, B. Fraboni, *Adv. Funct. Mater.* **2021**, *31*, 2009072.
- [37] H. Mescher, F. Schackmar, H. Eggers, T. Abzieher, M. Zuber, E. Hamann, T. Baumbach, B. S. Richards, G. Hernandez-Sosa, U. W. Paetzold, U. Lemmer, *ACS Appl. Mater. Interfaces* **2020**, *12*, 15774.
- [38] K. Legge, P. B. Greer, P. J. Keall, J. T. Booth, S. Arumugam, T. Moodie, D. T. Nguyen, J. Martin, D. J. O'connor, J. Lehmann, *J. Appl. Clin. Med. Phys.* **2017**, *18*, 358.
- [39] J. Zhao, L. Zhao, Y. Deng, X. Xiao, Z. Ni, S. Xu, J. Huang, *Nat. Photonics* **2020**, *14*, 612.
- [40] S. Demchyshyn, M. Verdi, L. Basiricò, A. Ciavatti, B. Hailegnaw, D. Cavalcoli, M. C. Scharber, N. S. Sariciftci, M. Kaltenbrunner, B. Fraboni, *Adv. Sci.* **2020**, *7*, 2002586.
- [41] D. Brivio, S. Albert, M. P. Gagne, E. Freund, E. Sajo, P. Zygmanski, *J. Phys. D: Appl. Phys.* **2020**, *53*, 265303.
- [42] S. Yakunin, M. Sytnyk, D. Kriegner, S. Shrestha, M. Richter, G. J. Matt, H. Azimi, C. J. Brabec, J. Stangl, M. V. Kovalenko, W. Heiss, *Nat. Photonics* **2015**, *9*, 444.
- [43] H. Hu, B. Dong, B. Chen, X. Gao, D. Zou, *Sustainable Energy Fuels* **2018**, *2*, 79.
- [44] X. Wang, S. A. Kulkarni, Z. Li, W. Xu, S. K. Batabyal, S. Zhang, A. Cao, L. H. Wong, *Nanotechnology* **2016**, *27*, 20LT01.
- [45] R. Li, X. Xiang, X. Tong, J. Zou, Q. Li, *Adv. Mater.* **2015**, *27*, 3831.
- [46] L. Qiu, J. Deng, X. Lu, Z. Yang, H. Peng, *Angew. Chem., Int. Ed.* **2014**, *53*, 10425.
- [47] J.-Y. Lam, J.-Y. Chen, P.-C. Tsai, Y.-T. Hsieh, C.-C. Chueh, S.-H. Tung, W.-C. Chen, *RSC Adv.* **2017**, *7*, 54361.
- [48] A. Babayigit, A. Ethirajan, M. Muller, B. Conings, *Nat. Mater.* **2016**, *15*, 247.
- [49] G. Schileo, G. Grancini, *J. Mater. Chem. C* **2021**, *9*, 67.
- [50] K. H. Wang, L. C. Li, M. Shellaiah, K. W. Sun, *Sci. Rep.* **2017**, *7*, 13643.
- [51] P. Wang, F. Zhang, S. Gao, M. Zhang, A. I. Kirkland, *Sci. Rep.* **2017**, *7*, 2857.
- [52] H. Shen, R. Nan, Z. Jian, X. Li, *J. Mater. Sci.* **2019**, *54*, 11596.
- [53] B. Wenger, P. K. Nayak, X. Wen, S. V. Kesava, N. K. Noel, H. J. Snaith, *Nat. Commun.* **2017**, *8*, 590.
- [54] S. Kasap, *Springer Handbook of Electronic and Photonic Materials*, Springer International Publishing, Cham **2007**.
- [55] Y. Du, S. Wan, M. Xie, Y. Xia, W. Yang, Z. Wei, Y. Zhu, Y. Hua, Z. Jin, D. Hong, Y. Tian, *J. Phys. Chem. Lett.* **2021**, *12*, 7106.
- [56] X. Zheng, W. Zhao, P. Wang, H. Tan, M. I. Saidaminov, S. Tie, L. Chen, Y. Peng, J. Long, W.-H. Zhang, *J. Energy Chem.* **2020**, *49*, 299.
- [57] G. L. Long, J. D. Winefordner, *Anal. Chem.* **1983**, *55*, 712A.
- [58] J. Billinger, R. Nowotny, P. Homolka, *Eur. Radiol.* **2010**, *20*, 1572.
- [59] D. R. Shearer, M. Bopaiah, *Health Phys.* **2000**, *79*, S20.
- [60] T. Roques, *Radiotherapy Dose Fractionation*, The Royal College of Radiologists, London **2019**.